

Scalable Terahertz Room Temperature Photoreceivers Based on Large-Area Hexagonal Boron Nitride and Graphene Heterostructures

Leonardo Viti, Osman Balci, Jincan Zhang, Adil Meersha, Andrea C. Ferrari, and Miriam S. Vitiello*

The development of scalable techniques for large-area growth of layered materials unlocks technological opportunities for the implementation of devices and components suitable for on-chip integration on photonic integrated platforms. Here, terahertz (THz) photoreceivers based on large-area hexagonal boron nitride/single-layer graphene (SLG)/hexagonal boron nitride heterostructures, prepared by chemical vapor deposition and realized by means of an industrially scalable method, are reported. The photo-thermoelectric sensors are integrated on-chip with planar antennas, on-chip radio frequency circuitry, a low-pass hammer-head filter and coplanar strip lines, combining nanosecond response time and large sensitivity. Room temperature responsivities of ≈ 4 V W $^{-1}$, with noise equivalent power ≈ 4 nWHz $^{-1/2}$ at high (2.86 THz) frequencies are reached, in a fully frequency-scalable architecture. This paves the way for multiplexed hyperspectral THz cameras and optical communication systems.

1. Introduction

Stacking layered materials (LMs) with different properties to create LM heterostructures (LMHs) enables the exploitation of parameters such as twist angle^[1] and thickness,^[2] without being limited by lattice matching conditions. The resulting LMHs bring novel functionalities for devices operating in underexploited frequency domains such as the far infrared (FIR), and particularly at terahertz (THz) frequencies (1–5 THz). LMHs consisting

L. Viti, M. S. Vitiello
NEST

CNR-Istituto Nanoscienze and Scuola Normale Superiore Piazza San Silvestro 12, Pisa 56127, Italy

E-mail: miriam.vitiello@sns.it

O. Balci, J. Zhang, A. Meersha, A. C. Ferrari Cambridge Graphene Centre University of Cambridge Cambridge CB3 0FA, UK

The ORCID identification number(s) for the author(s) of this article can be found under https://doi.org/10.1002/adom.202402100

© 2025 The Author(s). Advanced Optical Materials published by Wiley-VCH GmbH. This is an open access article under the terms of the Creative Commons Attribution License, which permits use, distribution and reproduction in any medium, provided the original work is properly cited.

DOI: 10.1002/adom.202402100

of single layer graphene (SLG) encapsulated with hBN layers were reported with mobility, μ , up to three million cm²V-¹s⁻¹ at room temperature (RT)[³] and were used to develop fast (800 ps response time, τ) and sensitive (noise equivalent power – NEP ≈100 pWHz⁻¹/²) photodetectors[⁴] and tunable electrical modulators.[⁵] hBN/black-phosphorus/hBN heterostructures were used for compact THz detectors,[6,7] demonstrating the activation of phonon-polariton modes on fs timescales.[8]

Despite the emergence of array-based commercial systems for FIR photodetection, [9–12] there is still a need for a photodetection platform that combines RT operation, sub-nanosecond speed, and a broad (0.1–4 THz) operational frequency range, to be used in imaging and communication applications. Commercial

microbolometers have a low noise equivalent power (NEP) $\approx\!30$ pWHz, $^{-1/2[13]}$ with a slow response time in the range $\approx\!10-1000\,\mu s.^{[14]}$ Complementary metal-oxide semiconductor (CMOS)-based field effect transistors (FETs) show $\tau\approx\!1$ ns $^{[15]}$ and their NEP decreases (63 pWHz $^{-1/2}$ at 2.5 THz) when reducing the gate lengths to 90 nm. $^{[16]}$ This hampers the device's cost-effectiveness, in particular for high (>2.5 THz) frequencies, where there is a significant interest in metrology, $^{[17]}$ optical and Gigabit data rate wireless communications, $^{[18,19]}$ high-resolution sensing, high-precision spectroscopy. $^{[20]}$ and tomography. $^{[21]}$

Graphene can be integrated with semiconductor-based technologies. [10,22] A key requirement for this is the development of industrial-scale, reliable, and inexpensive production processes. Graphene research has recently made enormous progress in material preparation and synthesis, utilizing both bottom-up techniques (graphene nanoribbons, graphene, and carbon nanomembranes) and top-down techniques. [23,24] For large-scale material production, various techniques have been implemented such as graphene growth on SiC, [25] growth on either metals or insulators by chemical vapor deposition (CVD) techniques. [23,26]

In the THz range, state-of-the-art performance was achieved in single-pixel ultrafast SLG thermoelectric photodetectors (PDs), with 800 ps response time at RT.^[27] These PDs used exfoliated SLG encapsulated with exfoliated hBN, with



www.advopticalmat.de

 μ = 50.000 cm²V⁻¹s⁻¹.^[4] However, micromechanically exfoliated flakes are not suitable for industrial requirements.

present photothermoelectric photodetection [28-30] at THz frequencies in graphene p-njunctions defined in large (cm²)-area hBN/SLG/hBN. This marks a significant milestone in the development of a fully scalable platform for FIR photodetection. The PTE mechanism enables zero-bias operation and typically dominates RT THz detection in graphene-based devices.[27,31] It takes advantage of the efficient carrier heating in SLG, stemming from the low ($\approx 10^{-19}$ J K⁻¹) electronic heat capacity,^[32] and from the high optical phonon energy ($\approx 0.2 \text{ eV}^{[33]}$). As a result, large (ΔT_e ≈1000 K) photo-induced gradients in the electronic temperature, $T_{\rm e}$, can be achieved, even with low energy (THz) photons. [34] These gradients are excited on ultrafast ($\approx 10 \text{ fs}^{[30]}$) timescales and the electronic heat is relaxed to the lattice by means of slower electron-phonon interactions,[35] with cooling times of few picosecond.[36] This ultrafast carrier thermodynamics enables high(sub nanosecond)-speed PTE detection, [27] ultimately limited by the electron cooling times.[30] The advantage of gate-voltage-defined p-n junction geometry, with respect to a standard single-top-gate FET, is that the Seebeck coefficients (S_b) on the two sides of the junction can be independently modified to maximize the photodetector response. The PTE voltage is defined as $V_{PTE} = (S_{bL} - S_{bR}) \times \Delta T_e$, where S_{bL} and S_{bR} are the Seebeck coefficients on the left and on the right of the junction, respectively.

1.1. Material Preparation and Characterization

Large (10 mm × 10 mm)-area hBN/SLG/hBN LMH is assembled as follows. SLG is initially grown in a hot wall CVD system using a $\approx 30 \,\mu\text{m}$ thick Cu foil as a substrate. The foil, suspended on a quartz holder and loaded into the CVD system, is annealed at 1050 °C for 2 h under H_2 gas (100 sccm) at 760 Torr and cooled down to RT. The foil is annealed at 1050 °C with 50 sccm hydrogen flow at 0.4 Torr for 2h. 5 sccm CH₄ is introduced to start growth, completed in 30 min by stopping the CH₄ flow. The system is then naturally cooled down to RT under 50 sccm H₂. Asgrown SLG/Cu is spin-coated with poly (methyl methacrylate) (PMMA) at 1000 rpm for 1 min and baked at 80 °C for 10 min. After etching SLG on the other side using mild oxygen plasma, PMMA-coated SLG/Cu is kept in water overnight to oxidize the Cu foil. PMMA/SLG is then electrochemically delaminated by applying 2V between the Pt anode and PMMA/SLG/Cu cathode in a NaOH aqueous electrolyte ($\approx 1 \,\mathrm{m}$). The PMMA/SLG stack is cleaned in water and transferred on the first hBN layer, then baked at 80 °C for 10 min after ≈10 h natural drying. PMMA is removed by soaking in acetone and isopropyl alcohol. The top and bottom layers of hBN, both 10 nm thick, corresponding to \approx 30 atomic layers, are grown on c-plane Al₂O₃ (0001) at 1400 °C, 500 mbar for 30 min in an AIXTRON CCS 2D reactor. 10 sccm N₂ is used to transport the single-source precursor, borazine, to the reactor. Before hBN growth, the sapphire substrates are annealed in H₂ for 5 min at 750 mbar and 1180 °C. As-grown hBN on cplane sapphire is then spin-coated with PMMA (950k molecular weight, 4% diluted in anisole) at 1000 rpm for 1 min and baked at $80~^\circ\text{C}$ for 10~min. PMMA-coated hBN on sapphire is kept in $\approx 8\%$ H $_3\text{PO}_4$ for $\approx 10~\text{h}$ to delaminate PMMA/hBN. LMHs are assembled through semi-dry transfer to get clean-SLG/hBN interface with the aid of PMMA and a cm-sized frame fabricated using kapton tape. To enhance the interaction between SLG and hBN, overnight baking (>10~\text{h} at $80~^\circ\text{C}$) is conducted after the transfer of each layer. SLG and hBN are then characterized by Raman spectroscopy. Raman spectra are acquired using a Renishaw Raman spectrometer, equipped with a 2400gr mm $^{-1}$ grating, $\times 100~$ 0 objective with a numerical aperture (NA) of 0.95 producing a spot size of $\approx 1~\mu\text{m}$. All spectra are recorded in ambient conditions at 514 nm with a incident laser power < 1~mW to avoid any laser heating.

Raman spectra of SLG are acquired at different positions for a statistical analysis. A typical Raman spectrum is shown in Figure 1a. The G peak is located at position $POS(G) = 1588.5 \pm 100$ 2.4 cm⁻¹ and the 2D peak at POS(2D) = 2690.8 ± 1.8 cm⁻¹. The 2D and G peaks are single Lorentzians with full-widht at half-maximum FWHM(2D) = 29.5 ± 0.4 cm⁻¹, and FWHM(G) = 14.2 ± 1.5 cm⁻¹. The 2D to G peak intensity and area ratios are $I(2D)/I(G) = 2.44 \pm 0.37$ and $A(2D)/A(G) = 5.06 \pm 0.24$. A small D peak at POS(D) = 1347.5 ± 6.4 cm⁻¹ is visible, with I(D)/I(G) = 0.01 ± 0.01 . A linear fit gives a slope $\Delta Pos(2D)/\Delta Pos(G) \approx 0.754$, indicating negligible strain.[37] We estimate the Fermi energy, obtaining^[38,39] $E_{\rm F} \approx 377 \pm 23$ meV and carrier concentration $n = (2.2 \pm 0.7) \times 10^{12} \text{ cm}^{-2} \text{ from A(2D)/A(G), I(2D)/I(G),}$ FWHM(G), Pos(G) and Pos(2D), with p-type doping. Finally, $n_D =$ $(5.1 \pm 1.3) \times 10^9$ cm⁻² is estimated from I(D)/I(G), E_F and excitation energy 2.41 eV.[40,41] In addition, we observe a 2D' peak located at 3250 cm $^{-1}$ \pm 1.9 cm $^{-1}$ that is the overtone of a double resonance process that can happen as an intravalley process and a two-phonon defect-assisted process, leading to the D + D' peak located at 2465 \pm 2.1 cm⁻¹.

A representative Raman spectrum of the hBN encapsulation layer is shown in Figure 1b. In all spectra, we observe a single peak of 1369 \pm 0.64 cm⁻¹, which corresponds to the E_{2g} phonon in hBN.^[42] The FWHM is 30.4 \pm 1.0 cm⁻¹. We then perform a statistical analysis acquiring Raman spectra on different positions of the fully encapsulated SLG after transfer. A representative spectrum is shown in Figure 1c. The same peaks of SLG are still visible, with a D peak probably merged with the E₂₀ optical phonon peak of hBN. Importantly, the G and 2D peaks shift and broaden, with the following values averaged over >20 spectra: POS(G) = 1584.6 \pm 1.4 cm⁻¹, POS(2D) = 2679.4 $\pm 3.9 \text{ cm}^{-1}$, FWHM(G) = 26.0 $\pm 2.5 \text{ cm}^{-1}$, and FWHM(2D) = 47.6 ± 2.3 cm⁻¹. We note that after encapsulation and transfer, graphene has changed from *p*-type doping to *n*-type doping, with an $E_{\rm F} \approx 110 \pm 30$ meV, and a corresponding electron concentration of $\approx (8.1 \pm 2.5) \times 10^{11}$ cm⁻². Furthermore, the analysis of the 2D-peak vs G-peak frequency in different positions on the sample (Figure 1d) reveals low doping, as confirmed in transport measurements, and moderate levels of strain, that we attribute to the roughness (≈3 nm) of the hBN-SLG-hBN heterostructure.[43,44] Improving the semi-dry transfer method could lead to reduced roughness, which, in turn, would decrease the strain in the graphene layer and the residual doping, as a consequence of the well-known correlation between strain and doping.[45]

21951071, 2025, 4, Downloaded from https://onlinelibrary.wiley.com/doi/10.1002/adom.202402100 by Socchow University, Wiley Online Library on [10/02/2025]. See the Terms and Conditi

and-conditions) on Wiley Online Library for rules of use; OA articles are governed by the applicable Creative Commons

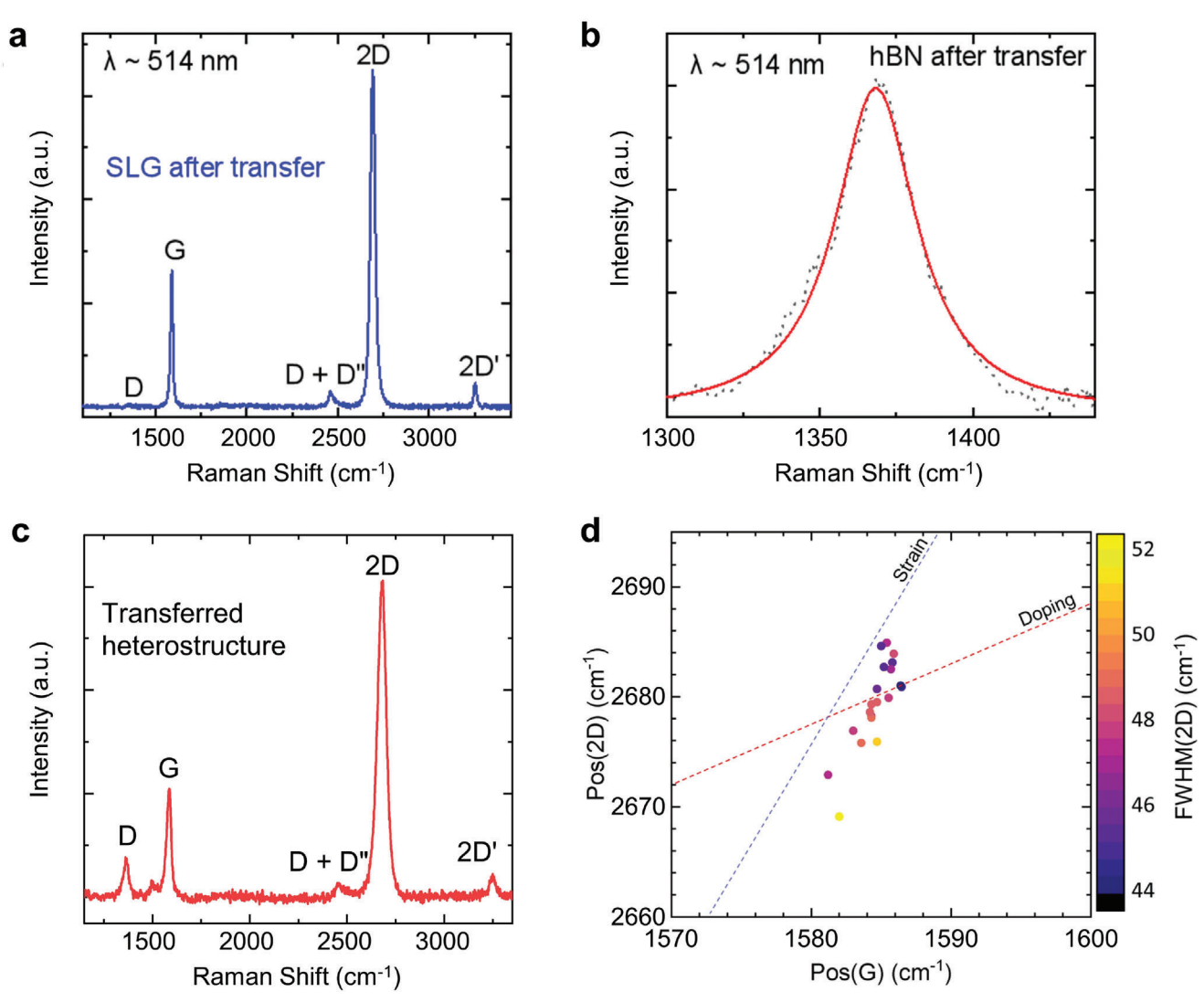


Figure 1. a) Raman spectrum of SLG at 514 nm prior to encapsulation with hBN. b) Raman spectrum of hBN layer. c) Raman spectrum of the transferred hBN-SLG-hBN heterostructure. d) 2D-peak vs G-peak frequency extracted from Raman spectra acquired in different positions on the sample. The color bar represents the values of FWHM(2D) in the recorded spectrum. The dispersion of the data points indicates the presence of tensile and compressive strain

1.2. Device Design and Fabrication

Graphene field-effect transistors (GFETs), exploiting large area hBN/SLG/hBN heterostructures, whose atomic force microscope (AFM) image is reported in **Figure 2a**, are then fabricated using a combination of electron beam lithography (EBL, Zeiss Ultra-Plus), atomic layer deposition (ALD, Oxford OpAL), and metal evaporation on a high resistivity $\mathrm{SiO}_2/\mathrm{Si}$ substrate.

The atomic structure of hBN gives it an inherent excellent thermal stability, high electrical insulation, and superior thermal conductivity, beneficial for stable RT performance, and thermal management, as well as for increasing graphene mobility.^[3]

The selected device geometry is a p-n junction, defined by top split-gates over an H-shaped channel, created through reactive ion etching (CF₄/O₂ mixture, 25 W, etch rate 3 nm s⁻¹). The source (s) and drain (d) electrodes are lithographically defined along the SLG channel at a relative distance $L_c = 2.0 \mu m$. The

size of the s and d ohmic contacts defines the channel width $W_c = 0.8 \mu m$. The fabrication process is completed by depositing 5/40 nm Cr/Au through thermal evaporation and liftoff. This gives 1D edge contacts^[46] to the SLG channel, with a contact resistance $R_0 \approx 10 \text{ k}\Omega$. Notably, this value is larger than the typical contact resistances observed for hBN-encapsulated SLG obtained by micromechanical cleavage, [46] but comparable to reported R₀ values obtained for CVD-grown large-area graphene samples with similar geometries.^[47,48] We ascribe this to suboptimal interfaces between hBN and SLG in our heterostructure, possibly caused by the roughness (≈3 nm) of the hBN/SLG/hBN stack. A layer of HfO₂ (\approx 30 nm thick, grown at 130 °C, relative permittivity $\varepsilon_r \approx$ 17^[49]) is then ALD-grown on the channels as the top-gate oxide. Top-gate (g) electrodes, with a gap separation \approx 200 nm, are finally realized by depositing 5/90 nm Cr/Au. In the p-n junction geometry, the asymmetry required for PTE generation is determined by the longitudinal variation of the SLG Seebeck coefficient



www.advopticalmat.de

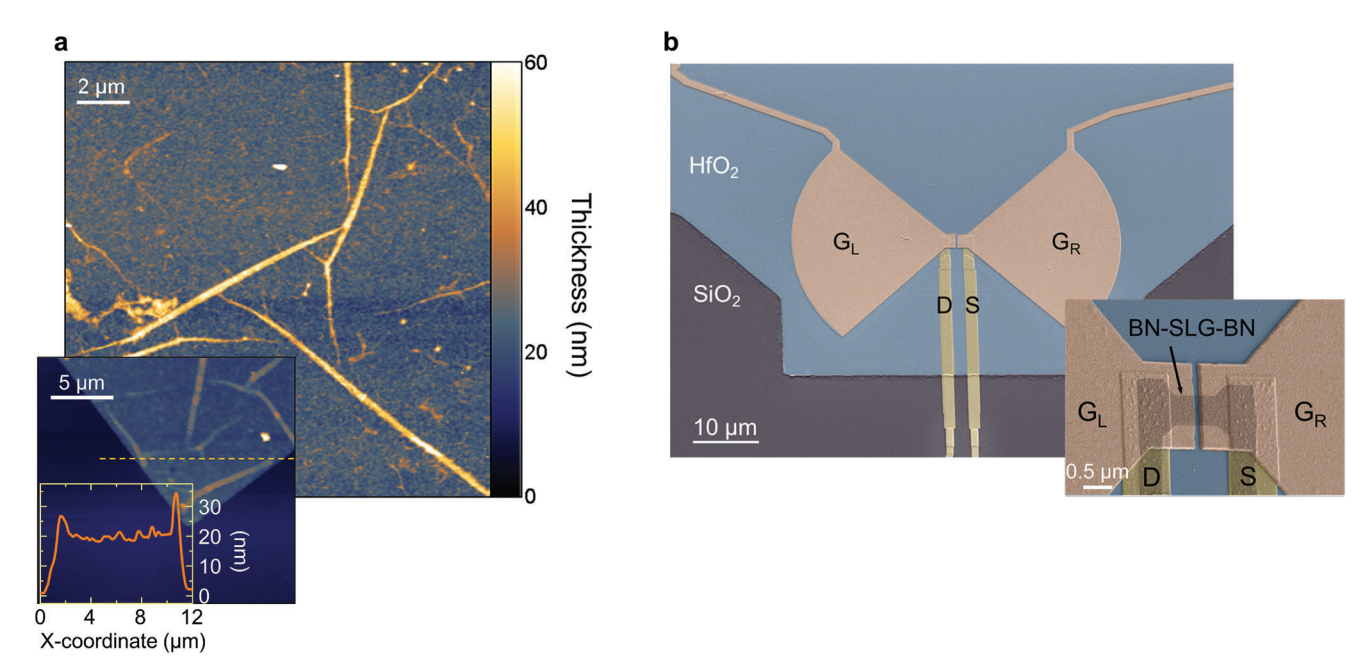


Figure 2. a) AFM image of the hBN/SLG/hBN heterostructure. Flat (roughness ≈ 3 nm) domains are surrounded by ≈ 100 nm thick wrinkles, forming during the transfer process. The inset shows the thickness profile of the heterostructure, measured near the edge of a square defined by reactive ion etching (horizontal dashed orange line) to expose the SiO₂ surface underneath. An average thickness of 20 nm is retrieved, corresponding to the sum of the thicknesses of the three layers constituting the stack. b) False color scanning electron microscope (SEM) image of complete p-n junction device, coupled to a bow-tie THz antenna. Inset: zoom on the SLG channel. The shaded area corresponds to the hBN/SLG/hBN heterostructure.

 (S_{bL}, S_{bR}) , whose profile along the channel can be electrostatically defined by applying distinct gate voltages (V_g) at the two gates on the left and right sides of the junction. To reduce the detector shunt capacitance, s and d electrodes are connected to a coplanar strip line, [27] defined as two parallel metallic strips on the substrate top surface. Figure 2b shows the false color scanning electron microscope (SEM) images of one of the fabricated devices (nine devices in total, five of them coupled to the planar on-chip THz antennas).

The gate electrodes are designed in the shape of two halves of a bow tie antenna, with a flare angle of 90° and a bow radius of 24 µm. At 2.86 THz and for normal incidence, the bow-tie geometry, with a gap separation of 200 nm, results in a field enhancement \approx 40 between the antenna branches, when the electromagnetic wave, polarized parallel to the antenna axis, reaches the detector from the air side. This is estimated using a finite element method (FEM) simulation of the antenna architecture, [47] through a commercial software (Comsol Multiphysics^[50]).

In our geometry, the antenna is not isolated from the surrounding circuit. Therefore, we also include a low-pass hammerhead filter along the coplanar strip line with a cutoff frequency $f_{\rm cut-off} \sim 300$ GHz, which enhances the isolation between antenna and readout circuit. It comprises a capacitive shunt with a lumped capacitance $C_{\rm f} = 500$ aF. The dimensions of the structure have been preventively optimized by time-domain simulations, following a previous report. [27]

2. Results and Discussion

The chips are then mounted on a dual inline package, and the PDs are wire-bonded to the external package. Samples are

electrically characterized in air, at RT, using voltage generators to independently provide voltage to the source-to-drain (V_{SD}) or gate electrodes ($V_{gL,R}$). The resistance (R) curve, measured as a function of V_g (left) is plotted in Figure 3a and fitted as $R=R_0+(L_c/W_c)\times (1/n_{2d}e\mu_{FE}),$ where R_0 is the contact resistance, μ_{FE} is the field-effect mobility, $n_{2d} = \{n_0^2 +$ $[C_g/e \cdot (V_g - V_{CNP})]^2$ ^{-1/2} is the carrier density, [51]</sup> C_g is the gatecapacitance per unit area, and $V_{\mbox{\scriptsize CNP}}$ is the charge neutrality point. In this case, $V_{CNP} = -1.29$ V. From the fit to $R(V_g)$ we can determine $\mu_{FE} = 830 \text{ cm}^2/\text{Vs}^{-1}$, and a residual carrier $n_0 =$ $2.7\times10^{12}~cm^{-2}.$ Figure 3b plots μ_{FE} as a function of estimated from transport measurements n_0 for all devices (additional transport characterization curves are shown in the Supporting Information). An increase of n_0 of a factor of 3 causes μ_{EF} reduction of more than one order of magnitude. We note that the obtained values of mobility are still slightly subpar with respect to those obtained in recent reports on CVD graphene.[31,47,48] We ascribe this observation to the relatively high strain in the encapsulated SLG layer,[52] as it results from Raman characterization.

For the optical characterization, the antenna axis is oriented parallel to the linearly polarized electric field. As a pumping source, we adopt a single-mode quantum cascade laser (QCL) emitting at 2.86 THz, based on a single plasmon waveguide, mounted in a Stirling cooler and operating at 27 K in pulsed mode with 4% duty cycle. The beam is focused by two tsupurica (TPX) lenses onto a circular spot with radius $\approx\!200\,\mu\text{m}$. The corresponding average intensity at the focal point is $I_0=0.8\,\text{W}\,\text{cm}^{-2}$. We use a square-wave envelope with frequency $f_{\rm mod}=1.333\,\text{kHz}$ as a lock-in reference and as a triggering signal for the QCL pulse trains.

21951071, 2025, 4, Downloaded from https://onlinelibrary.wiley.com/doi/10.1002/adom.202402100 by Soochow University, Wiley Online Library on [10.022025]. See the Terms and Conditions (https://onlinelibrary.wiley.com/doi/10.1002/adom.202402100 by Soochow University, Wiley Online Library on [10.022025]. See the Terms and Conditions (https://onlinelibrary.wiley.com/doi/10.1002/adom.202402100 by Soochow University, Wiley Online Library on [10.022025]. See the Terms and Conditions (https://onlinelibrary.wiley.com/doi/10.1002/adom.202402100 by Soochow University, Wiley Online Library on [10.022025]. See the Terms and Conditions (https://onlinelibrary.wiley.com/doi/10.1002/adom.202402100 by Soochow University, Wiley Online Library on [10.022025]. See the Terms and Conditions (https://onlinelibrary.wiley.com/doi/10.1002/adom.202402100 by Soochow University, Wiley Online Library on [10.022025].

-conditions) on Wiley Online Library for rules of use; OA articles are governed by the applicable Creative Commons License

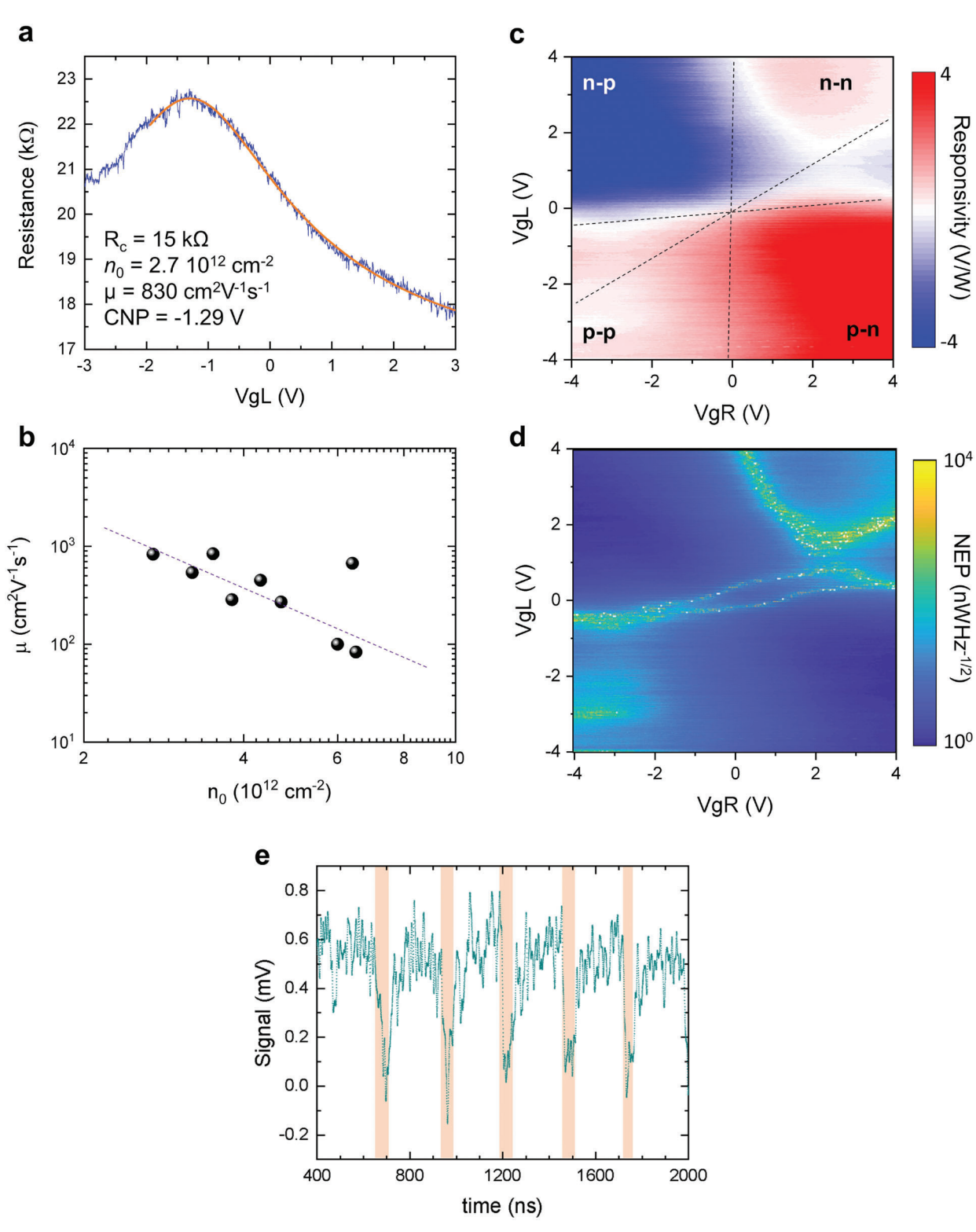


Figure 3. a) Resistance as a function of the gate voltage applied to the left side of the p-n junction. Experimental data in blue, fitting curve in orange. This plot is obtained with $V_{SD} = 2$ mV. b) μ_{FE} as a function of residual carrier density for nine GFETs, estimated from transport measurements. The dashed line is a guide for the eye, indicating the correlation between the two parameters. c) Gate-dependent responsivity showing a six-fold pattern typical of PTE response. Dashed lines are guides to the eye. d) NEP map as a function of the two gates. Regions where the responsivity vanishes in (c) correspond to regions where the NEP diverges in (d). e) Waveform of the photodetector's output recorded with an oscilloscope, when the QCL is operated at high voltage, corresponding to an intermittent output power. Intensity fluctuations are recorded by the receiver, whose bandwidth can be calculated by exponential fits to the charge/discharge times. Orange-shaded areas represent the time intervals in which the THz power is off.



www.advopticalmat.de

To extrapolate the PD responsivity, R_v , we extract the photovoltage (Δu) at the d electrode, while keeping s grounded (see Supporting Information). We employ a voltage preamplifier (DL Instruments, M1201, gain $\gamma=1000$) to amplify Δu and we send the signal to a lock-in (Stanford Research, 5210). Δu is then retrieved from the demodulated lock-in signal (V_{LI}) as $\Delta u=(\pi\times\sqrt{2/2})V_{LI}/\gamma$, where the pre-factor $\pi\times\sqrt{2/2}$ takes into account that the lock-in measures the RMS of the fundamental Fourier component of the square wave produced by the QCL modulation. R_v is then calculated from the ratio between Δu and the power $P_a=I_0A_{\rm eff}$ impinging on the detector, with $A_{\rm eff}$ the detector effective area, assumed equal to the diffraction-limited area, $I_{\rm eff}^{\rm S3} = I_{\rm eff}^{\rm S3} = I_{\rm eff}^{\rm S3} = I_{\rm eff}^{\rm S3}$, where $I_{\rm eff}^{\rm S3} = I_{\rm eff}^{\rm S3}$, where $I_{\rm eff}^{\rm S3} = I_{\rm eff}^{\rm S3}$, where $I_{\rm eff}^{\rm S3} = I_{\rm eff}^{\rm S3}$, where $I_{\rm eff}^{\rm S3} = I_{\rm eff}^{\rm S3}$, where $I_{\rm eff}^{\rm S3} = I_{\rm eff}^{\rm S3}$, where $I_{\rm eff}^{\rm S3} = I_{\rm eff}^{\rm S3}$, where $I_{\rm eff}^{\rm S3} = I_{\rm eff}^{\rm S3}$, where $I_{\rm eff}^{\rm S3} = I_{\rm eff}^{\rm S3}$, where $I_{\rm eff}^{\rm S3} = I_{\rm eff}^{\rm S3}$

Figure 3c displays R_v vs V_{gL} and V_{gR} for a typical p-n junction. It exhibits a distinct six-fold pattern, characteristic of a dominant PTE response.^[27,54] This arises from the non-monotonic dependence of the Seebeck coefficient with respect to E_{E} in SLG, tuned across the Dirac point by the electrostatic gating applied to the left and right sides of the junction (see Supporting Information for further details). This results in multiple sign changes in R_v. A maximum responsivity of 4 V W⁻¹ is observed at RT in Figure 3c. The corresponding NEP is in Figure 3d. We measure the noise spectral density (NSD) using a lock-in amplifier (Zurich Inst., UHFLI), while keeping the s electrode grounded and collecting the signal at the *d* electrode, while sweeping the modulation frequency. The NSD measured at 1.333 kHz is then used to calculate NEP (Figure 3d) as a function of the voltages applied to the gate electrodes. We achieve a minimum NEP ≈ 4 nWHz^{-1/2}, similar to that of other material platforms based on CVD-SLG.[47,48]

We characterize the speed of the devised photodetectors by measuring their response in the time domain. We employed an intermittent emission state of the QCL at high driving voltage to generate reproducible power fluctuations with a time constant <1 ns. [48] We record the output waveforms of the receiver with a fast oscilloscope (4 GHz bandwidth). For this measurement, we use a fast trans-impedance pre-amplifier (Femto, DHPCA, bandwidth 80 MHz, gain 10^4 VA $^{-1}$). Figure 3e shows one of the waveforms, measured with a QCL pulse duration of 1.6 μ s. The detection response time is evaluated by an exponential fit to the data (see Supporting Information), obtaining $\tau = 4.6 \pm 0.1$ ns, which corresponds to a bandwidth of 34 MHz. We note that this represents a lower bound for the device bandwidth, since the estimation of τ can be influenced by the waveform signal-to-noise ratio (SNR).

Figure 4 plots NEP vs n_0 to compare the PDs reported in refs. [4,27,47,48], characterized at 2.86 THz. This shows a correlation between lower NEPs with lower n_0 , explained by the increase in Seebeck coefficient, [48] and subsequent improvement in PTE response, when n_0 decreases.

Figure 4 also compares the performances of PDs based on micromechanically cleaved (MC) SLG with those made with large-area crystals. $^{[4,27,47,48]}$

3. Conclusion

Although MC samples define the state of the art, our results indicate that it is possible to achieve SLG-hBN encapsulation over a large (1 cm²) area with performances compatible with commercial expensive (up to 10 000 euro) technologies at high (>3THz)

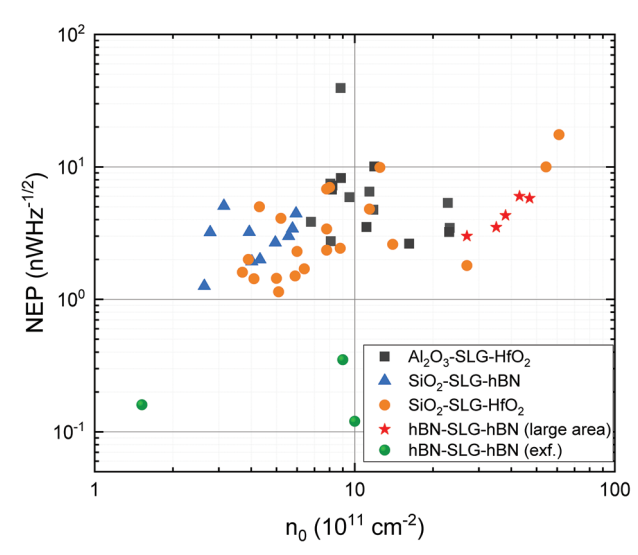


Figure 4. NEP at 2.86 THz as a function of n_0 for various SLG-based material platforms.^[4,27,47,48]

frequencies. This opens up promising opportunities for device enhancement through stacking optimization, while maintaining scalability and compatibility with CMOS processing, as crucial for industrial applications.

In summary, we reported THz PDs with $R_{V}{>}1~VW^{-1}$ and NEP $\approx 5~nWHz^{-1/2}$ at 2.86 THz. By scaling the antenna bow radius from $\approx 0.5~mm$ to $\approx 10~\mu m$ the device can operate in a fully frequency scalable range, from 0.3 THz up to 6 THz, $^{[48,54-56]}$ respectively, i.e., where the commercial electronic sources or the recent generation of high-frequency QCLs operates. Indeed, the operational frequency of our devices is only set by the specific dimensions and shape $^{[57]}$ of the on-chip patterned planar antennas, making the presented technological approach very versatile. Finally, the short response time of these detectors makes them particularly suitable for short-range ($\approx 10~m$) THz communication applications.

The scalable multi-pixel architectures enabled by this technology are of great interest for real-time imaging applications, such as process and quality control, biomedicine, and cultural heritage preservation, as well as for integrated photonic platforms for quantum applications.

Supporting Information

Supporting Information is available from the Wiley Online Library or from the author.

Acknowledgements

This work was supported by the European Research Council through the ERC project Terascan (101157731), and by the European Union – Next Generation EU under the Italian National Recovery and Resilience Plan (NRRP), Mission 4, Component 2, Investment 1.3, CUP B53C22003970001, partnership on "Telecommunications of the Future" (PE00000001 – program "RESTART," Structural Project DREAMS, Focused project T-Next), the Graphene Flagship, ERC Grants Hetero2D, GIPT, EU Grants GRAP-X, CHARM, EPSRC Grants EP/K01711X/1, EP/K017144/1, EP/N010345/1, EP/L016087/1, EP/V000055/1, EP/X015742/1.

OPTICAL MATERIALS

www.advopticalmat.de

Open access publishing facilitated by Consiglio Nazionale delle Ricerche, as part of the Wiley - CRUI-CARE agreement.

Conflict of Interest

The authors declare no conflict of interest.

Code Availability

The codes and simulation files that support the plots and data analysis within this paper are available from the corresponding author upon reasonable request.

Data Availability Statement

The data that support the plots within this paper and other finding of this study are available from the corresponding authors upon reasonable request

Keywords

larga area bi dimensional materials, photodetectors, terahertz

Received: August 6, 2024 Revised: December 31, 2024 Published online: January 25, 2025

- [1] R. Bistritzer, A. H. MacDonald, *Proc. Natl. Acad. Sci. USA* 2011, 108, 12233
- [2] A. K. Geim, I. V. Grigorieva, Nature 2013, 499, 419.
- [3] L. Banszerus, M. Schmitz, S. Engels, J. Dauber, M. Oellers, F. Haupt, K. Watanabe, T. Taniguchi, B. Beschoten, C. Stampfer, Sci. Adv. 2015, 1, 1500222.
- [4] L. Viti, D. G. Purdie, A. Lombardo, A. C. Ferrari, M. S. Vitiello, *Nano Lett.* 2020, 20, 3169.
- [5] A. Di Gaspare, E. A. A. Pogna, L. Salemi, O. Balci, A. R. Cadore, S. M. Shinde, L. Li, C. di Franco, A. G. Davies, E. H. Linfield, A. C. Ferrari, G. Scamarcio, M. S. Vitiello, Adv. Funct. Mater. 2021, 31, 2008039.
- [6] L. Viti, J. Hu, D. Coquillat, A. Politano, C. Consejo, W. Knap, M. S. Vitiello, Adv. Mater. 2016, 28, 7390.
- [7] W. Guo, Z. Dong, Y. Xu, C. Liu, D. Wei, L. Zhang, X. Shi, C. Guo, H. Xu, G. Chen, L. Wang, K. Zhang, X. Chen, W. Lu, Adv. Sci. 2020, 7, 1907609
- [8] M. A. Huber, F. Mooshammer, M. Plankl, L. Viti, F. Sandner, L. Z. Kastner, T. Frank, J. Fabian, M. S. Vitiello, T. L. Cocker, R. Huber, Nat. Nanotechnol. 2017, 12, 207.
- [9] F. H. L. Koppens, T. Mueller, P. Avouris, A. C. Ferrari, M. S. Vitiello, M. Polini, Nat. Nanotechnol. 2014, 9, 780.
- [10] M. Romagnoli, V. Sorianello, M. Midrio, F. H. L. Koppens, C. Huyghebaert, D. Neumaier, P. Galli, W. Templ, A. D'Errico, A. C. Ferrari, Nat. Rev. Mater. 2018, 3, 392.
- [11] Rigi Camera. https://www.swissterahertz.com/, (accessed: October 2024).
- [12] Terahertz Compact Cameras., https://ticwave.com/ (accessed: October 2024).
- [13] F. Simoens, J. Meilhan, *Philos. Trans. R. Soc. A* **2014**, *372*, 20130111.
- [14] F. Sizov, Semicond. Sci. Technol. 2018, 33, 123001.
- [15] K. Ikamas, A. Lisauskas, S. Boppel, Q. Hu, H. G. Roskos, J. Infrared, Millimeter, Terahertz Waves 2017, 38, 1183.

- [16] A. Lisauskas, M. Bauer, S. Boppel, M. Mundt, B. Khamaisi, E. Socher, R. Venckevicius, L. Minkevicius, I. Kasalynas, D. Seliuta, G. Valusis, V. Krozer, H. G. Roskos, J. Infrared, Millimeter, Terahertz Waves 2014, 35, 63.
- [17] E. Riccardi, V. Pistore, L. Consolino, A. Sorgi, F. Cappelli, R. Eramo, P. De Natale, L. Li, A. G. Davies, E. H. Linfield, M. S. Vitiello, *Laser Photonics Rev.* 2023, 17, 2200412.
- [18] A. Sorgi, M. Meucci, M. A. Umair, F. Cappelli, G. Toci, P. De Natale, L. Viti, A. C. Ferrari, M. S. Vitiello, L. Consolino, J. Catani, *Laser Photonics Rev.* 2024, https://doi.org/10.1002/lpor.202301082.
- [19] A. Montanaro, G. Piccinini, V. Mišeikis, V. Sorianello, M. A. Giambra, S. Soresi, L. Giorgi, A. D'Errico, K. Watanabe, T. Taniguchi, S. Pezzini, C. Coletti, M. Romagnoli, *Nat. Commun.* 2023, 14, 6471.
- [20] E. Riccardi, V. Pistore, S. Kang, L. Seitner, A. De Vetter, C. Jirauschek, J. Mangeney, L. Li, A. G. Davies, E. H. Linfield, A. C. Ferrari, S. Dhillon, M. S. Vitiello, *Nat. Photon.* 2023, 17, 607.
- [21] J. P. Guillet, B. Recur, L. Frederique, B. Bousquet, L. Canioni, I. Manek-Hönninger, P. Desbarats, P. Mounaix, J. Infrared Millim. Terahertz Waves 2014, 35, 382.
- [22] M. A. Giambra, V. Mišeikis, S. Pezzini, S. Marconi, A. Montanaro, F. Fabbri, V. Sorianello, A. C. Ferrari, C. Coletti, M. Romagnoli, ACS Nano 2021, 15, 3171.
- [23] F. Bonaccorso, A. Lombardo, T. Hasan, Z. Sun, L. Colombo, A. C. Ferrari, Mater. Today 2012, 15, 564.
- [24] C. Backes, N. Kubetschek, S. Goldie, 2D Mater. 2020, 7, 022001.
- [25] W. A. De Heer, C. Berger, M. Ruan, M. Sprinkle, X. Li, Y. Hu, Z. Baiqian, J. Hankinson, E. Conrad, Proc. Natl. Acad. Sci. USA 2011, 108, 16900.
- [26] X. Li, W. Cai, L. Colombo, R. S. Ruoff, Nano Lett. 2009, 9, 4268.
- [27] L. Viti, A. R. Cadore, X. Yang, A. Vorobiev, J. E. Muench, K. Watanabe, T. Taniguchi, J. Stake, A. C. Ferrari, M. S. Vitiello, *Nanophotonics* 2021, 10, 89
- [28] N. M. Gabor, J. C. W. Song, Q. Ma, N. L. Nair, T. Taychatanapat, K. Watanabe, T. Taniguchi, L. S. Levitov, P. Jarillo-Herrero, *Science* 2011, 334, 648.
- [29] J. C. W. Song, M. S. Rudner, C. M. Marcus, L. S. Levitov, *Nano Lett.* 2011, 11, 4688.
- [30] M. Massicotte, G. Soavi, A. Principi, K.-J. Tielrooij, Nanoscale 2021, 13, 8376
- [31] F. Ludwig, A. Generalov, J. Holstein, A. Murros, K. Viisanen, M. Prunnila, H. G. Roskos, ACS Appl. Electron. Mater. 2024, 6, 2197.
- [32] M. A. Aamir, J. N. Moore, X. Lu, P. Seifert, D. Englund, K. C. Fong, D. K. Efetov, *Nano Lett.* **2021**, *21*, 5330.
- [33] S. Piscanec, M. Lazzeri, F. Mauri, A. C. Ferrari, J. Robertson, Phys. Rev. Lett. 2024, 93, 185503.
- [34] I. Iliakov, A. Ponomaryov, D. Saleta Reig, C. Murphy, J. D. Mehew, T. V. A. G. de Oliveira, G. L. Prajapati, A. Arshad, J.-C. Deinert, M. F. Craciun, S. Russo, S. Kovalev, K.-J. Tielrooij, *Nano Lett.* 2023, 23, 3872.
- [35] M. Lazzeri, C. Attaccalite, L. Wirtz, F. Mauri, Phys. Rev. B 2008, 78, 081406.
- [36] E. A. A. Pogna, X. Jia, A. Principi, A. Block, L. Banszerus, J. Zhang, X. Liu, T. Sohier, S. Forti, K. Soundarapandian, B. Terrés, J. D. Mehew, C. Trovatello, C. Coletti, F. H. L. Koppens, M. Bonn, H. I. Wang, N. van Hulst, M. J. Verstraete, H. Peng, Z. Liu, C. Stampfer, G. Cerullo, K.-J. Tielrooij, ACS Nano 2021, 15, 11285.
- [37] T. M. G. Mohiuddin, A. Lombardo, R. R. Nair, A. Bonetti, G. Savini, R. Jalil, N. Bonini, D. M. Basko, C. Galiotis, N. Marzari, K. S. Novoselov, A. K. Geim, A. C. Ferrari, *Phys. Rev. B* 2009, 79, 205433.
- [38] A. Das, S. Pisana, B. Chakraborty, S. Piscanec, S. K. Saha, U. V. Waghmare, K. S. Novoselov, H. R. Krishnamurthy, A. K. Geim, A. C. Ferrari, A. K. Sood, *Nat. Nanotechnol.* 2008, 3, 210.
- [39] D. M. Basko, S. Piscanec, A. C. Ferrari, Phys. Rev. B 2009, 80, 165413.
- [40] M. Bruna, A. K. Ott, M. Ijäs, D. Yoon, U. Sassi, A. C. Ferrari, ACS Nano 2014. 8, 7432.



ADVANCED OPTICAL MATERIALS

www.advancedsciencenews.com

www.advopticalmat.de

- [41] L. G. Cançado, A. Jorio, E. H. Martins Ferreira, F. Stavale, C. A. Achete, R. B. Capaz, M. V. O. Moutinho, A. Lombardo, T. S. Kulmala, A. C. Ferrari, Nano Lett. 2011, 11, 3190.
- [42] S. Reich, A. C. Ferrari, R. Arenal, A. Loiseau, I. Bello, J. Robertson, Phys. Rev. B 2005, 71, 205201.
- [43] L. Belyaeva, C. Ludwig, Y.-C. Lai, C.-C. Chou, C.-J. Shih, Small 2024, 20, 2307054.
- [44] L. Lin, B. Deng, J. Sun, H. Peng, Z. Liu, Chem. Rev. 2018, 118, 9281.
- [45] T. Vincent, V. Panchal, T. Booth, S. R. Power, A.-P. Jauho, V. Antonov, O. Kazakova, 2D Mater. 2019, 6, 015022.
- [46] L. Wang, I. Meric, P. Y. Huang, Q. Gao, Y. Gao, H. Tran, T. Taniguchi, K. Watanabe, L. M. Campos, D. A. Muller, J. Guo, P. Kim, J. Hone, K. L. Shepard, C. R. Dean, *Science* 2013, 342, 614.
- [47] M. Asgari, E. Riccardi, O. Balci, D. De Fazio, S. M. Shinde, J. Zhang, S. Mignuzzi, F. H. L. Koppens, A. C. Ferrari, L. Viti, M. S. Vitiello, ACS Nano 2021, 15, 17966.
- [48] M. Asgari, L. Viti, O. Balci, S. M. Shinde, J. Zhang, H. Ramezani, S. Sharma, A. Meersha, G. Menichetti, C. McAleese, B. Conran, X. Wang, A. Tomadin, A. C. Ferrari, M. S. Vitiello, Appl. Phys. Lett. 2022, 121, 031103.

- [49] A. Paghi, S. Battisti, S. Tortorella, G. De Simoni, F. Giazotto, ArXiV 2024, https://doi.org/10.48550/arXiv.2407.04501.
- [50] COMSOL AB, COMSOL Multiphysics ν. 6.2, COMSOL AB, Stockholm, Sweden.
- [51] S. Kim, J. Nah, I. Jo, D. Shahrjerdi, L. Colombo, Z. Yao, E. Tutuc, S. K. Banerjee, Appl. Phys. Lett. 2009, 94, 062107.
- [52] L. Wang, P. Makk, S. Zihlmann, A. Baumgartner, D. I. Indolese, K. Watanabe, T. Taniguchi, C. Schönenberger, Phys. Rev. Lett. 2020, 124, 157701
- [53] E. Javadi, D. B. Bu, K. Ikamas, J. Zdanevičius, W. Knap, A. Lisauskas, Sensors 2021, 21, 2909.
- [54] S. Castilla, B. Terrés, M. Autore, L. Viti, J. Li, A. Y. Nikitin, I. Vangelidis, K. Watanabe, T. Taniguchi, E. Lidorikis, M. S. Vitiello, R. Hillenbrand, K.-J. Tielrooij, F. H. L. Koppens, *Nano Lett.* 2019, 19, 2765.
- [55] L. Vicarelli, M. S. Vitiello, D. Coquillat, A. Lombardo, A. C. Ferrari, W. Knap, M. Polini, V. Pellegrini, A. Tredicucci, *Nat. Mater* 2012, 11, 865.
- [56] A. Zak, M. A. Andersson, M. Bauer, J. Matukas, A. Lisauskas, H. G. Roskos, J. Stake, *Nano Lett.* 2014, 14, 5834.
- [57] Y. Shi, X. Zhang, Q. Qiu, Y. Gao, Z. Huang, IEEE Access 2021, 9, 113823.